Molecular dynamics simulations of ionic concentration gradients across model bilayers

Jonathan N. Sachs[a)]
Department of Biomedical Engineering, The Johns Hopkins University School of Medicine, Baltimore, Maryland 21205

Horia I. Petrache
Laboratory of Physical and Structural Biology, NICHD, National Institutes of Health, Bethesda, Maryland 20892

Daniel M. Zuckerman
Center for Computational Biology and Bioinformatics, School of Medicine, University of Pittsburgh, Pittsburgh, Pennsylvania 15213

Thomas B. Woolf[b)]
Department of Biomedical Engineering, The Johns Hopkins University School of Medicine, Baltimore, Maryland 21205 and Department of Physiology, The Johns Hopkins University School of Medicine, Baltimore, Maryland 21205

To model a concentration gradient across a biomembrane, we have performed all-atom molecular dynamics simulations of NaCl solutions separated by two oppositely charged plates. We have employed the recently formulated three-dimensional Ewald summation with correction (EW3DC) technique for calculations of long-range electrostatics in two-dimensionally periodic systems, allowing for different salt concentrations on the two sides of the plates. Six simulations were run, varying the salt concentrations and plate surface charge density in a biologically relevant range. The simulations reveal well-defined, atomic-level asymmetries between the two sides: distinct translational and rotational orderings of water molecules; differing ion residency times; a clear wetting layer adjacent only to the negative plate; and marked differences in charge density/potential profiles which reflect the microscopic behavior. These phenomena, which may play important roles in membrane and ion channel physiology, result primarily from the electrostatics and asymmetry of water molecules, and not from the salt ions. In order to establish that EW3DC can accurately capture fundamental electrostatic interactions important to asymmetric biomembrane systems, the CHARMM force-field (with the corrected Ewald sum) has been used. Comparison of the results with previously published simulations of electrolyte near charged surfaces, which employed different force-fields, shows the robustness of the CHARMM potential and gives confidence in future all-atom bilayer simulations using EW3DC and CHARMM. © 2003 American Institute of Physics.
[DOI: 10.1063/1.1531589]

I. INTRODUCTION

Understanding the behavior of ions and water near the pores of ion channels, in the so-called electrical double-layer, is of prime importance in elucidating ion channel function. Ion channels are among the most important transmembrane proteins involved in signal transduction. Among the many functional questions raised by ion channel researchers is how ion selectivity is achieved. One hypothesis is that the removal of waters from ion-hydration shells, as is required for ion conductivity, may be the rate-limiting step in selectivity.[1] Therefore, it becomes necessary to understand the structural and dynamic properties of hydrated ions, especially at the membrane–electrolyte interface. The importance of studying ion and water behavior at the membrane surface is further highlighted by experimental data on lipid headgroup conformational dynamics. The degree to which ions disrupt hydra-

tion shell structure—which is sensitive to ion type and charge—affects fluctuations in headgroup structure.[2,3] Bilayer structural properties, including headgroup dynamics, influence transmembrane protein structure and function,[4–9] and thus we must understand the behavior of hydrated ions near these surfaces.

Despite the complexity of the membrane–electrolyte interface[7]—which includes proteins, lipids, water, and salt—there are concrete properties of this region which may be exploited in constructing models of the membrane. For example, it has been well established that functional properties of ion channels, such as conductance level, are quite sensitive to bilayer surface charge, which is biologically regulated via the ratio of charged to uncharged lipids. This has been shown extensively in the gramicidin A channel,[10–12] the alamethicin channel,[13] and K^+ channels.[14] Further, models of bilayers need not be symmetric, as biological membranes are known to be asymmetric in lipid composition, and hence in charge density. The asymmetric lipid distribution could be due to a different ratio of negative phosphatidylserine (PS)

a)Electronic mail: jsachs@bme.jhu.edu
b)Electronic mail: woolf@groucho.med.jhmi.edu

and neutral phosphatidylcholine (PC) lipids in the two leaflets. This, in principle, leads to an asymmetry in local ordering of water and salt in the double-layer, which could have profound consequences for the biophysical processes involved in transmembrane signaling. In addition, one recognizes that the water molecule itself is asymmetric, both in geometry and in partial charge distribution. The nonspherical, asymmetric nature of water molecules at the surface of membranes may play a significant role in influencing headgroup conformations, as well as in determining the strength of interactions between headgroups and ions. Finally, differences in ionic radii may influence the balance of enthalpic and entropic constraints on hydration shell structure, and may thus play a significant role in membrane protein structure and function.

Experimentally, related questions regarding the influence of molecular level interactions, dynamics, and structure can be addressed using spectroscopic and scattering methods.[15,16] In addition, theoretical treatment has provided insight.[17,18] Supplementing these techniques are computational simulations, which provide atomic-level descriptions. Both Monte Carlo[19] and molecular dynamics (MD)[20–26] simulations have been used extensively to study the behavior of water and salt next to both charged and uncharged surfaces. Surface charge density and molecular roughness have been shown to affect the orientational distribution of water molecules. These parameters are directly related to the charge state and chemical structure of lipid headgroups, and thus are relevant to studies of biomembranes. There is extensive literature devoted to MD simulations of biomembranes[27–33] and transmembrane proteins, including ion channels.[34–39] All-atom representation of the bilayer, however, is computationally expensive, and hence prohibitive for exploring new methodologies. It has been shown that reduced representations of the bilayer—which are computationally more efficient than all-atom representations—can provide important insight into fundamental properties dictating the biophysical nature of membrane systems. For example, it has been shown that a lattice of inducible dipoles can be used to represent the electrostatic environment and for calculations of transmembrane protein solvation free energies.[40] The work presented here utilizes MD to simulate a model transmembrane concentration gradient, in which the membrane is represented as two oppositely charged surfaces. Such a reduced representation allows for efficient investigation of the detailed behavior of water and salt in this novel, biologically relevant geometry.

Because all-atom simulations that cut off electrostatic interactions have well known artifacts,[41–44] including severe reductions of salt mobility, we apply the Ewald summation technique. One methodological aspect of simulations that utilize the Ewald sum is that the system must be replicated periodically in all three dimensions. Simulations of a transmembrane concentration gradient have two-dimensional periodicity, and thus have not been previously performed. One solution would be to simulate more than one bilayer per unit cell, but this is currently computationally prohibitive. The problem of simulating systems with two-dimensional periodicity has been similarly challenging for simulations of electrical double layers between oppositely charged
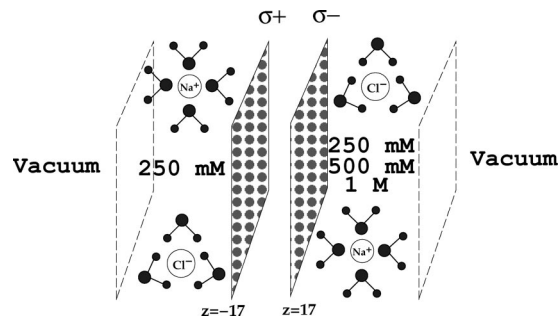

FIG. 1. Schematic of system setup. Two plates composed of discrete vdW spheres (see Methods) are separated by 34 Å of empty space. Concentrations on the negative plate side are varied (see Table I), while they are kept constant at 250 mM on the positive plate side in all systems. Vacuum regions are placed at the ends of the electrolyte regions to allow for application of the EW3DC technique for calculation of electrostatic interactions. Excess counterions are added, making each side (including the plate) electrically neutral.

electrodes.[23–26,45,46] A rigorously convergent two-dimensional Ewald sum (EW2D) does exist, and is thought to be the ideal method for long-range electrostatic calculations in such systems.[47–49] While simulations utilizing this method have been shown to give good agreement with experimental results,[50] the implementation of EW2D is prohibitively slow.[23,51,52] One successful alternative adds a shape-dependent correction term[53,54] to the traditional Ewald sum. The corrected method (EW3DC) and EW2D have demonstrated quantitative agreement.[24,55] Because the implementation of EW3DC was found to be ten times faster, we adopt it here. The increase in computational efficiency is crucial for studies of large systems such as biological membranes.

It is important to note that the effectiveness of EW3DC applied to a bilayerlike setting, as is presented here, has yet to be tested. Among the goals of this study is to show that fundamental properties of the system, such as water order and hydration, are correctly calculated under the CHARMM force-field with EW3DC. Methodologically, the work represents an important modification to previous simulations[19,20,24,55,56,] as it applies the EW3DC technique to a more biologically relevant geometry, incorporating a concentration gradient in which electrolyte species interact across a model bilayer. As is discussed below, the model bilayer consists of charged Lennard-Jones spheres, facilitating efficient evaluation of the effectiveness of EW3DC through a comparison of our results with these other related systems. Having shown the viability of simulations in this geometry, it is believed that application of the EW3DC methodology should prove valuable in future all-atom simulations of biological membranes solvated by electrolyte.

We present here simulations of two NaCl solutions separated by two oppositely charged plates, as shown in Fig. 1. The system is constructed to mimic bilayer geometry, with disparate salt concentrations (in the range of 250 mM to 1M) on the two sides of the plates. The plates are separated by 34 Å, the approximate width of a typical biological membrane.[57] The choice of oppositely charged plates models an asymmetric distribution of lipid types between opposed

monolayers. The plates consist of a square lattice of tightly packed van der Waals (vdW) spheres, which also carry point charges at their centers, modeling both the roughness of a bilayer surface and the discreteness of charge. The surface charge values were chosen to approximate that of biological membranes, in the range of 0 C/m^2 to 0.2 C/m^2, which corresponds to a biologically realistic ratio of charged to uncharged lipids.

Water ordering (both translational and orientational), ion distributions, and electrostatic potential profiles are analyzed as functions of plate surface charge density and salt concentration. We find asymmetric ordering of water molecules at the two plates, which is explained as a manifestation of the geometric and electrostatic asymmetry of the water molecule itself. Specific interactions between the oppositely charged hydrogens and oxygens, with the oppositely charged plates, lead to better defined water layers and hydration shell structure on the negative plate side, both of which are in accordance with previously published results.[20–22] Simulation details are presented in the next section, followed by results for water and salt ordering, as well as electrostatic potential profiles in Sec. III. A discussion of the asymmetries in these molecular orderings follows in Sec. IV.

II. METHODS

A. Simulation setup

Figure 1 shows the general setup for the simulations. In order to establish the viability and efficacy of applying EW3DC to membrane systems, the design of the system was chosen to match as closely as possible that of Crozier *et al.*[55] with the intention of comparing the results against those of an electrodelike system. The cathode, or negatively charged plate, was placed at $z = +17$ Å, while the anode, or positively charged plate, was placed at $z = -17$ Å. Each 25.5 Å× 25.5 Å plate was a 17×17 lattice of tightly packed vdW spheres of radius 0.75 Å. Single point charges were placed at the center of each sphere, the magnitude of which were determined by the overall plate surface charge density, $\pm \sigma$. The position of the spheres was fixed throughout the simulations. Adjacent to each plate, electrolyte regions were built, each extending 42.5 Å from the plates, making the total volume of each electrolyte region 27 636 Å^3. Vacuum regions 2.5 times the cumulative length of the electrolyte and plate regions were placed adjacent to the electrolyte regions. Thus the overall dimensions of the simulation cell were 25.5 Å×25.5 Å×714 Å. In all simulations the total number of particles (waters, Na$^+$ and Cl$^-$) per side was kept constant at 1000.

Four classes of simulation are presented, distinguished by the value of σ, as shown in Table I. Class $\sigma = 0$ C/m^2 was a system with neutral plates, while the plates were charged in classes $\sigma = \pm 0.05$ C/m^2, $\sigma = \pm 0.1$ C/m^2, and $\sigma = \pm 0.2$ C/m^2. The ionic concentration on the positive plate side was held constant at 250 mM for all classes. Class $\sigma = 0.1$ C/m^2 consisted of three separate sets of simulations, in which the negative plate side concentration was set to either 250 mM, 500 mM, or 1 M. These correspond to 4, 8, and 16 ions, respectively. Excess counterions were added to each side

TABLE I. Configurational parameters for the six sets of simulations presented. Four classes of system are defined based upon the plate surface charge density. Positive plate side ionic concentrations were fixed at 250 mM, while the negative plate side concentrations were varied as shown. Three simulations with $\sigma = 0.1$ C/m^2 provided information regarding the effect of changing negative plate side concentration. Note that, as described in the text, excess counterions were added to each side in the non-neutral plate systems.

σ_{plate}	Positive plate side			Negative plate side			[NaCl]
	N_{Wat}	N_{Na^+}	N_{Cl^-}	N_{Wat}	N_{Na^+}	N_{Cl^-}	
0.0 C/m^2	992	4	4	992	4	4	250 mM
± 0.05 C/m^2	990	4	6	990	6	4	250 mM
± 0.1 C/m^2	988	4	8	988	8	4	250 mM
± 0.1 C/m^2	988	4	8	980	12	8	500 mM
± 0.1 C/m^2	988	4	8	964	20	16	1 M
± 0.2 C/m^2	984	4	12	984	12	4	250 mM

which neutralized the charge on the plate. However, unlike with an ideal parallel plate capacitor, in which the external electric fields are zero everywhere, the discreteness of the plate charges and the explicit treatment of the electrolyte solutions allows for interactions between the two sides and affects their dynamics. This *trans*-bilayer interaction is influenced by the concentration gradient and is therefore unique among systems previously described.[19,20,24,26,58] However, the time-averaged structure approaches that of isolated sides in the long time limit. Thus, while the system presented here does capture side–side interactions on short time scales assumed relevant to biomembrane dynamics, the long time average structure should be comparable with simulations of electrolytes confined within parallel plates.

Electrolyte regions were prepared by starting with two pre-equilibrated water boxes (100 ps of dynamics with no salt), followed by a random placement of ions within each box, each ion replacing a water molecule. The system was constructed as described above, and the whole system was then subject to a minimization and dynamics (110 ps) cycle for further equilibration. Ten starting configurations were constructed for each system presented, with the initial ion placements varying between them. Data were averaged over all ten configurations, and over 1 ns of dynamics per configuration. Hence, a total of 10 ns of dynamics is presented for each setup. Simulations were performed using CHARMM software,[59] version 26. Periodic boundary conditions were used with constant number of atoms (N), temperature (T $= 298$ K), and volume (V) to generate NVT ensembles. A cutoff of 12 Å was used for van der Waals interactions. The time step was 2 fs, and all bonds involving hydrogens were fixed using the SHAKE algorithm, with a tolerance (relative deviation) of 10^{-6}. The frequency of regenerating the nonbonded list was set with a heuristic testing algorithm that updates based on the distance each atom moved since the last update.

CHARMM utilizes the TIP3P water model[60] which consists of three partially charged sites, and agrees well with experimental data regarding hydration and energetics. The parameterization of the ions was based upon comparison with solvation free energy data and quantum mechanical calculations.[58] The CHARMM parameterization has been

extensive[61,62] and in addition to small molecule quantum calculations is focused upon biomolecular interactions (e.g., water–protein, water–lipid and lipid–lipid interactions).

In order to use EW3DC, we made a modification to the CHARMM implementation of the particle mesh Ewald (PME) sum following Yeh *et al.*[24] to account for the two-dimensional periodicity. Following previous work,[23,24] we tested this implementation by calculating the force acting between two oppositely charged point charges as a function of separation distance. As with previous results, the resulting force profile plateaud at long separations under the current implementation of EW3DC, but diverged under EW3D. Such consistency with previous results showed that the current implementation was reliable. The method also required placement of vacuum regions in the z-dimension, in order to reduce interactions between the two boundaries. In order to insure that waters did not evaporate into the vacuum regions, a force was applied using a miscellaneous mean field potential (MMFP).[63] This acted at the water–vacuum boundary, inhibiting evaporation and also minimizing artifactual ordering.

We have run 10 ns of dynamics for each of the setups presented in Table I, a total of 60 ns for the work presented here. As discussed below, the $\sigma=0$ C/m^2 simulations consist of two perfectly symmetric sides. In the case of perfect sampling, therefore, we expect the properties of these two sides to be the same. As shown below, this is in fact the case, and we take this as evidence that 10 ns is indeed sufficient simulation time for each system. Each configuration (1 ns) was run for 65 h on 8 processors of an IBM SP3.

B. Density and electrostatic potential profiles

Average number density profiles of water and salt, as a function of distance from the plates, were calculated as follows. Each electrolyte region was divided into volumetric slices of length 0.2 Å in the z-dimension. A histogram of z positions was then constructed as a trajectory averaged quantity for water hydrogen and oxygens, as well as for Na$^+$ and Cl$^-$. Number densities are therefore in units of atoms/Å^3. Normalized ionic concentration profiles were obtained by dividing by bulk concentrations.

Poisson's equation gives the electrostatic potential, $\Phi(z)$, as

$$\nabla^2 \Phi(z) = -\frac{1}{\epsilon_0} \rho_c(z) \tag{2.1}$$

with $\rho_c(z)$ being the charge density distribution. Thus, an integration of $\rho_c(z)$ can yield the potential profile, $\Phi(z)$. Spohr[23] used the following form in order to calculate $\Phi(z)$,

$$\Phi(z) = -\frac{1}{\epsilon_0} \int_0^z \rho_c(z')(z-z')dz', \tag{2.2}$$

which is the form utilized in this work.

C. Residency times

In order to investigate the local dynamic behavior of ions near the plates, residency times for ions, τ, at a given z position were calculated from fits to the time correlation function

$$\langle N(t+\Delta t)\rangle_t = \langle N(t)\rangle_t \exp\left(-\frac{\Delta t}{\tau}\right), \tag{2.3}$$

where $N(t)$ is the number of ions present at time t and $N(t+\Delta t)$ is the number of ions still present at time $t+\Delta t$. The brackets indicate averaging over all time frames within the simulation. As was done in Ref. 64, the z-dimension was broken into 4 Å regions, and the average z for that region is given in the plots.

D. Volumetric calculations

Calculation of thermally accessible volumes for the water and ions was done using a Voronoi procedure provided by Gerstein *et al.*[65] Briefly, given a distribution of atoms, the standard Voronoi procedure constructs a polyhedron around each atom, that has the property that all interior points are closer to the central atom than to any others. The resulting partitioning fills the entire space in the simulation box (i.e., allows no voids). The reported volumes are averages over trajectories and configurations.

III. RESULTS

Table I lists the simulation details for the four classes of system presented here. For simplicity, we adopt a nomenclature as follows: for example, $\sigma=0$ C/m^2 (250 mM, 1 M) refers to the system which has positive plate side concentration of 250 mM, and negative plate side concentration of 1 M. In what follows, we present the trajectory averaged results for the six sets of simulations. We first provide results for macroscopic and microscopic water properties, followed by salt properties, including evidence that the EW3DC technique has enabled appropriate salt mobility. Finally, we present the macroscopic electrostatic potential profiles, which results from the combined properties of the water and salt.

A. Water ordering

As we will discuss the interactions between the solvent (water) and solute (salt) with the plates, we first present the distribution profiles for water. Figure 2(A) shows the water number density profile, $n(z)$, for the neutral plates simulation ($\sigma=0$ C/m^2), with hydrogen, $n_{hyd}(z)$, and oxygen, $n_{oxy}(z)$, shown separately. Data are presented as a function of distance from the charged plates (negative distances for the positively charged plate side are simply meant to reflect the geometry of the system). Hydrogen distribution tails approach the plates roughly 1 Å closer than do those for oxygen. Two strong peaks are seen in the plots, followed by a third less clear peak. These oscillations are due to local ordering of the waters, as known from experimental measurements and previous simulations.[20,24,55,66] Typically, the peaks are used to define water hydration layers. Beyond approxi-
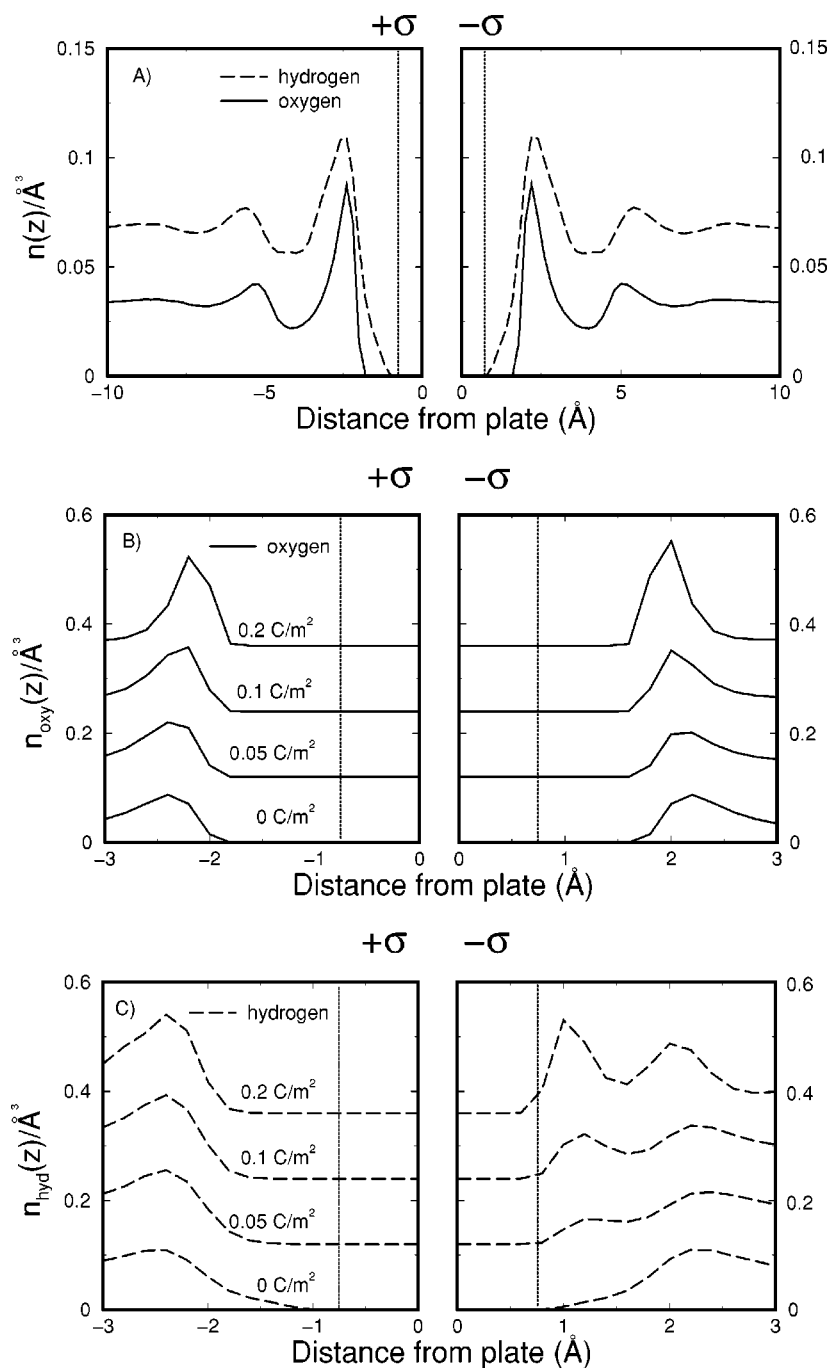
FIG. 2. Effect of plate surface charge density, σ, on oxygen $n_{oxy}(z)$ and hydrogen $n_{hyd}(z)$ number density profiles. Note that the bulk water density is 0.0334 waters/$Å^3$. (A) For $\sigma=0.0$ C/m^2, oxygen (solid line) and hydrogen (dashed line) profiles. (B) The first oxygen peaks for $\sigma=0.0$ C/m^2, ± 0.05 C/m^2, ± 0.1 C/m^2, and ± 0.2 C/m^2. (C) The first hydrogen peaks, systems as in (B). Data in parts (B) and (C) have been shifted up for clarity. The vertical, dotted black line indicates the position of the surface of the plate vdW spheres, at $z=0.75$ Å.

mately 10 Å from each plate, the profiles reach a constant value, signaling no influence from the plates. Thus, for simplicity, data is presented only out to 15 Å from each plate.

Consistent with previous simulations,[55] water number density profiles are relatively insensitive to the varied concentration of salt on the negative plate side in the $\sigma=\pm$ 0.1 C/m^2 simulations (data not shown). However, these densities vary quite profoundly with changing the plate charge σ. Thus, we next consider the effect of σ on these profiles, and focus on the first water layer. Figure 2(B) shows that as σ is increased from 0 to $\pm$ 0.2 C/m^2, the peak positions remain relatively constant. Increasing σ has a more profound effect on the hydrogen profiles. Figure 2(C) shows that there is an additional structure in the first hydrogen layer on the negative plate side, seen in the emergence of a second peak ap-

proximately 1 Å closer to the plate than the original peak. No such second peak is seen on the positive plate side.

There are two factors which determine the shapes of the distributions shown in Fig. 2, namely, the relative position of water molecules and their relative orientation. The latter influences the hydrogen distributions, $n_{hyd}(z)$, more profoundly, as is now discussed. We observe that the distance between the two hydrogen peaks on the negative plate side is less than the 1.6 Å hydrogen–hydrogen (HH) distance for each water molecule. This suggests that the HH vector is in average tilted with respect to z, meaning there is a σ induced reorientation of the water. Previous simulations of water near platinum surfaces[20] showed clear, electrostatically induced orientations of water molecules near surfaces. These simulations used a different water model and potential function
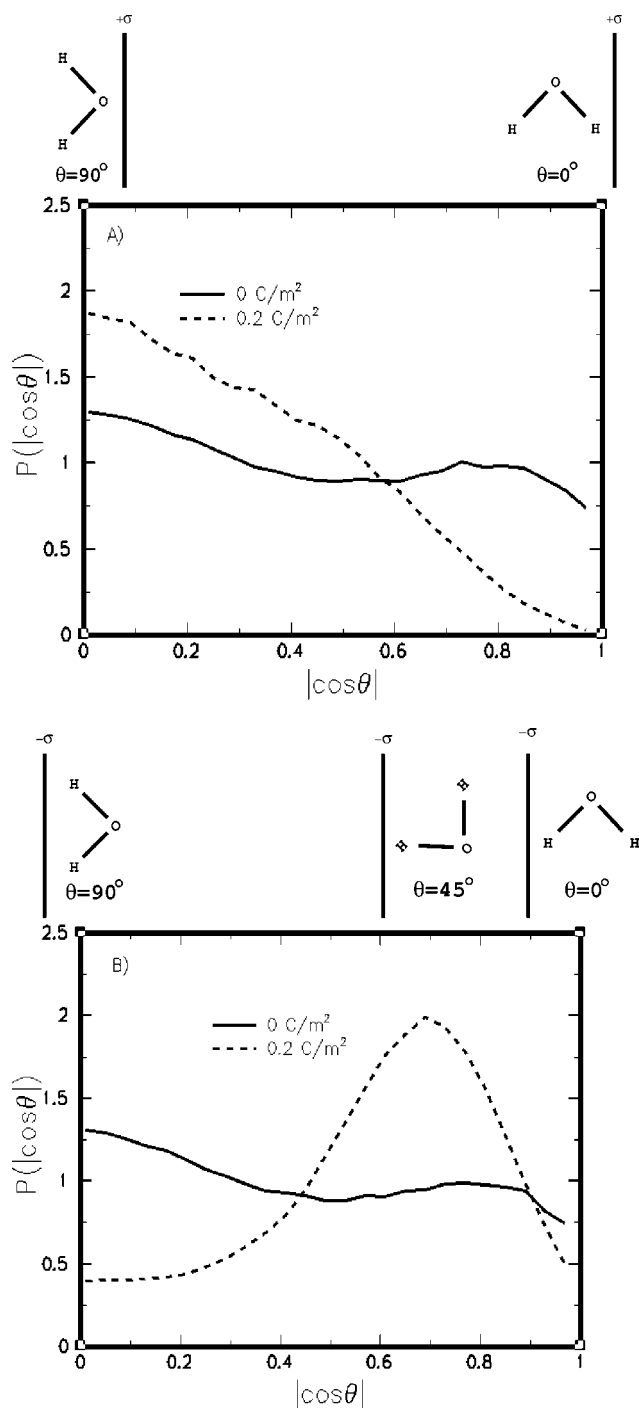
FIG. 3. Effect of σ on the orientation of first layer water molecules, as given by the probability distribution of $|\cos \theta|$, the angle between the HH vector and the z-axis, for (A) the positive plate side and (B) the negative plate side. $\sigma=0.0$ C/m^2 (solid line) and $\sigma=\pm 0.2$ C/m^2 (dashed line) are shown. Data is binned in 0.2 Å increments. Corresponding water orientations are shown for illustrative purposes. Note that the distribution for a bulk, isotropic water under no influence from the plates is a flat line.

than is employed here. However, comparison with these results is informative. As such, the distributions P(cos θ) of angles θ between the HH vector and the z-axis for waters in the first water layers next to the plates are plotted in Fig. 3. Corresponding water orientations for $\theta=0°$ (perpendicular), 45°, and 90° (parallel) are shown for illustrative purposes. Note that there is an inherent ambiguity in the definition at

$\theta=90°$, in that the water molecule plane (defined by the OH bonds) can be either parallel or perpendicular to the plate. The distribution for bulk water, that is at locations away from the plates, is expected to be flat. Thus, we can understand the shapes of these distributions in each case in terms of deviations from the bulk case. Starting with the neutral plate case, the distributions on both sides are identical, and are clearly not flat, suggesting that the plates have introduced restrictions in the orientational freedom of the waters. This is most likely due to excluded volume effects, since the plates bear no charge. There is a greater probability of the HH vector being parallel to the plate ($\theta=90°$) than perpendicular ($\theta=0°$), which is geometrically consistent with the presence of only one hydrogen peak in the profiles shown in Fig. 2. The distributions P(cos θ) are quite broad, with significant probability of the HH vector being perpendicular to the plate.

Next we focus on the effects of charging the plates ($\sigma \neq 0$), starting with the positive plate side [Fig. 3(A)]. The maximum value for P(cos θ) is still at 90°, but population of this state has increased, while the $\theta=0°$ state has become less populated with the increase in σ. This indicates an electrostatically induced restriction in rotational freedom for the waters. Figure 3(B) shows the distribution for the negatively charged plate side. Increasing σ generates a maximum of P(cos θ) at $\theta=45°$ (waters tilted away from the plates), consistent with previous simulations.[19] This preferred orientation generates the double peak in $n_{hyd}(z)$ shown before in Fig. 2(C). The average position of this peak is shifted *towards* the $\theta=90°$ orientation with increasing σ (data not shown). Interestingly, the orientation of these water molecule next to the negative plate reflects an atomic-scale double-layer *within* the first water layer comprising the more typically described ionic double-layer. Data for intermediate surface charge densities is omitted for clarity, but interpolate between the extremes. These results are in remarkable agreement with previous simulations,[20] endowing an at least moderate degree of confidence in the EW3DC/CHARMM potential.

We have seen that water molecules next to the plates pack differently than in bulk. We further investigated this by calculating the thermally accessible volumes of the water molecules utilizing the Voronoi algorithm (see Methods). Figure 4 shows the results of these calculations, for $\sigma=0$ and $\sigma=\pm 0.2$ C/m^2, as a function of distance from the plates. The figure highlights the volumetric restriction imposed upon the water molecules as they approach the plates, with the available volume decreasing by approximately 30% at 1 Å from the plates, essentially approaching the steric packing limit[67] (shown by the dashed lines in Fig. 4). On the negative plate side, increasing σ induces a decrease in relative water volume near the plates. There is, on the other hand, minimal volumetric response on the positive plate side. Data from the $\sigma=\pm 0.05$ and ± 0.1 C/m^2 cases is omitted but follows the trends shown.

B. Salt properties

Having shown the results for the solvent (water) behavior, we now turn to the solute (salt). The results for salt are presented in two sections. The first section gives time aver-
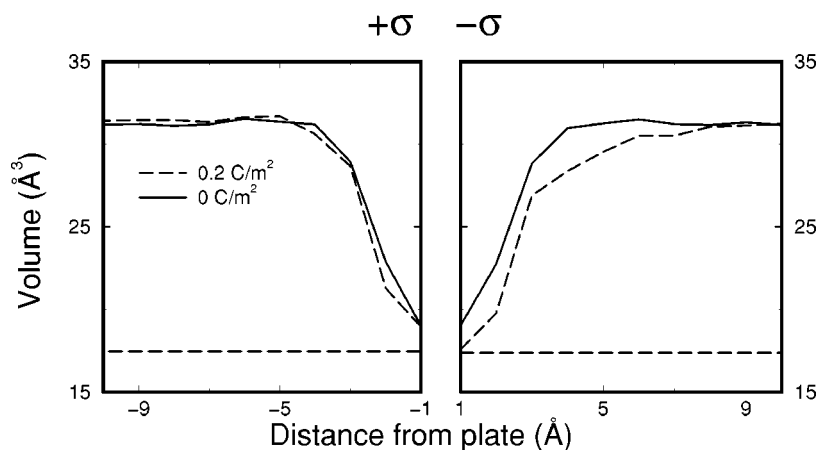
FIG. 4. There is a decrease in the thermally accessible volumes per water molecule near the plates, which is σ dependent on the negative plate side only. Calculated via the Voronoi procedure (see Methods), these volumes are plotted as a function of distance (in z) from the plates for $\sigma=0$ C/m^2 (solid line) and $\sigma=\pm\ 0.2$ C/m^2 (dashed line). Horizontal dashed lines indicate water bare volume (steric limit).

aged results, in the spirit of those presented above for the water. The second section gives time dependent results, in order to address the mobility of the salt.

1. Spatial distribution

In order to show the effects of σ on salt behavior, we have plotted the position dependent counter-ion concentrations for the $\sigma=\pm0.05$ C/m^2, $\sigma=\pm0.1$ C/m^2 and $\sigma=\pm0.2$ C/m^2 cases in Fig. 5. Note that the absolute distance of each counterion type from its corresponding plate is plotted. All counterion profiles show two well-defined layers. The position of the peaks is different for the two counterion types between the two sides, with the Cl$^-$ peak being approximately 0.8 Å closer to the positive plate than the Na$^+$ peak is to the negative plate. The first Cl$^-$ peak is larger in magnitude than the first Na$^+$ peak, while this trend is reversed for the second peaks. As opposed to the counterions, we see no intervening peaks in co-ion density on either side. Bulk concentrations are reached by approximately 20 Å from the plate for both ion types. Peak heights increases dramatically as σ is increased, and peak positions are shifted such that counte-

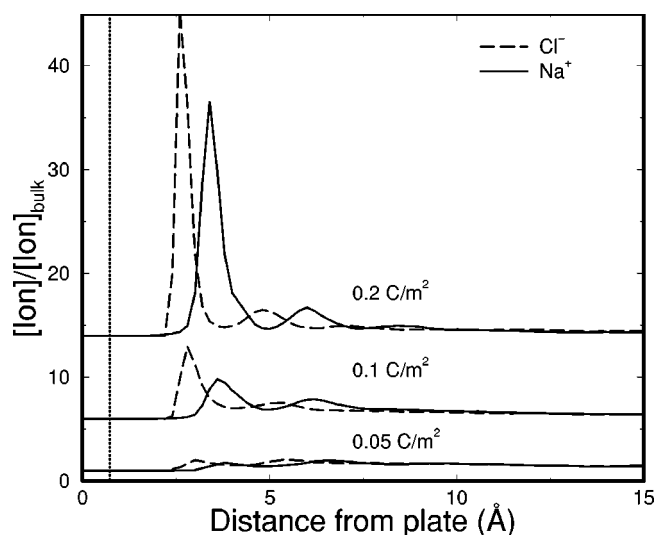rions approach closer to the more highly charged plates. In the case of neutral plates ($\sigma=0$) there is no peak in the ion distributions next to the plates (data not shown). Similar to the water, increasing the NaCl concentration on the negative plate side changes neither the peak heights nor the peak positions, as we have tested for all three $\sigma=0.1$ C/m^2 simulations (data not shown).

2. Range of motion

As mentioned in the Introduction, salt mobility has been of concern for MD simulations. Among the motivations for the use of the Ewald sum in calculating long-range electrostatics is the fact that under cutoffs there are thought to be artifacts in salt mobility.[41–44] Thus, it was necessary to verify mobility of ions in the simulations. Figure 6 shows a typical time series for the z-position of an arbitrarily selected Na$^+$ and Cl$^-$ on (A) the negative plate side and (B) the positive plate side from the $\sigma=\pm0.1$ C/m^2 (250 mM, 250 mM) simulations. Due to the vdW exclusion radii of the plate spheres, no particle can penetrate closer than approximately 0.75 Å plus its vdW radius from each sphere. Because the plate is rough, there are "dimpled" regions between the spheres where particles may get closer than this. The figure shows a clear ion exclusion zone of approximately 3.0 Å from the plates, attributed to an intervening water layer. The figures also show that co-ions freely traverse the z-dimension, populating the entire range in less than 1 ns. Counterions, on the other hand, have a tendency to adsorb to the plate for short periods, as expected.[26] Similar mobility is observed in the x- and y-dimensions and in all six simulated systems (data not shown).

In order to quantitatively characterize the adsorption phenomena, ion residency times, τ, were calculated (see Methods) and are shown in Fig. 7. For both Na$^+$ and Cl$^-$, there is a peak in τ located 4 Å from the plates, which is roughly 1 Å from the exclusion zone. Peak residency time for Na$^+$ next to the negative plate (273 ps) is greater than that of Cl$^-$ (171 ps) next to the positive plate, each approximately one order of magnitude less than the length of the simulation. Both Figs. 6 and 7 demonstrate, however, that the adsorption of counterions is a transient process within the simulations, as ions are not permanently bound to the surface. The falloff of τ to zero beyond the adsorption zone is

FIG. 5. Effect of σ on counterion concentration profiles. Solid lines are for Na$^+$ ions on the negative plate side and dashed lines are for Cl$^-$ ions on the positive plate side. Note that the distances are shown as absolute values, and data has been shifted up for clarity.
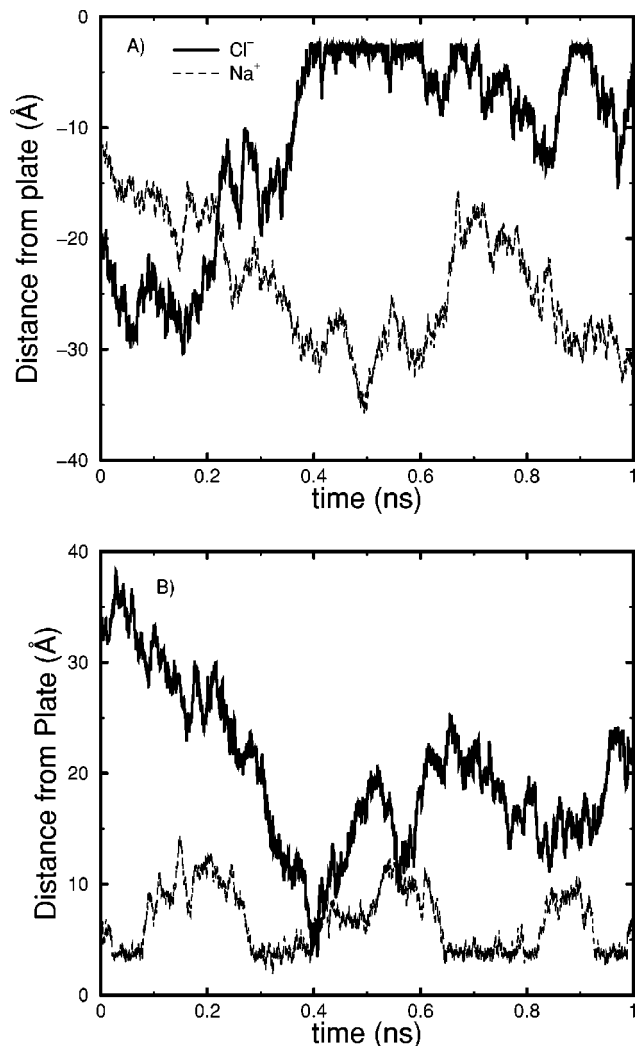
FIG. 6. Time series of distance from the plates for two arbitrarily selected Na$^+$ (thin, dashed line) and Cl$^-$ (thick, solid line) ions showing a wide range of ionic mobility under EW3DC. (A) the positive plate side and (B) the negative plate side of the $\sigma=0.1$ C/m^2 (250 mM, 250 mM) simulation. Similar motions are seen for all other systems, as well as for the x- and y-dimensions.

quite rapid, due to less restricted ion mobility in these regions. Similarly, co-ions (data not shown) have uniformly low residency times.

C. Electrostatic potential

Understanding atomic level ordering of waters and ions provides a unique backdrop for interpretation of macroscopic measurements such as the electrostatic potential. Having examined the properties of water and salt individually, we now turn to the charge density distribution as a whole. Figure 8 shows first layer charge distributions, $\rho_c(z)$, for $\sigma=0$ C/m^2 and $\sigma=\pm 0.2$ C/m^2. Results for $\sigma=0$ C/m^2 are, as expected, symmetric for the two sides. The results for $\sigma=\pm0.2$ C/m^2, however, are asymmetric, with the negative plate side showing more and better-defined alternating positive and negative peaks. On the negative plate side, the peaks of $\rho_c(z)$ closest to the plate are positive, and based on the hydrogen number density, $n_{hyd}(z)$ [see Fig. 2(C)], are most likely due to hydrogen. Note that this first peak, which is approximately 1 Å

in width, has a broad shoulder which is a manifestation of the double peak in $n_{hyd}(z)$. The first peak in $\rho_c(z)$ on the positive plate side is positive, due to the fact that hydrogens approach the plate more closely than oxygens. This trend is reduced as σ increases to 0.2 C/m^2, though it is not fully absent even in that high charge case. For $\sigma=\pm0.2$ C/m^2 there are two additional, well-defined water layers on the negative plate side (data not shown), which are absent on the positive plate side.

Using Eq. (2.2), we can now calculate electrostatic potential profiles, $\Phi(z)$, which are given in Fig. 9(A). Again, oscillations result from the molecular ordering discussed above. Results for $\sigma=0$ C/m^2 are perfectly symmetric. As was the case with $n_{hyd}(z)$ and $n_{oxy}(z)$, the potential is insensitive to changes in the negative plate side NaCl concentration. The positions of the first peak and valley in the negative plate side potential profiles correspond exactly with the first and second hydrogen number density peaks. The peaks and valleys for the positive plate side are less coincident. It will be seen that this is due to a more well-defined counterion hydration layer on the negative plate side.

In order to compare the potential profiles on the two sides, we choose to calculate the potential drop from the center of the plate vdW spheres to the bulk. In principle, one could also choose the surface of the spheres as the starting point for the calculation. Choosing the $z = 0$ point accounts for the possibility of atomic penetration into the dimpled regions of the lattice. It should be noted that this choice, while affecting the magnitude of the potential drop, $\Delta\Phi(z)$, did not affect the underlying asymmetry in the data. Figure 9(B) plots $\Delta\Phi(z)$ from each plate to the bulk as a function of σ. The change in magnitude of the drop is more than double on the positive plate side. As discussed above, there is an exclusion zone immediately adjacent to the plates, and therefore the potential changes linearly over this region. The difference in the overall potential drop is due to the different molecular ordering on the two sides. The length of the exclusion zone on each side, which is less for the negative plate and is defined by the vdW ''roughness'' of the plate surface and the vdW radii of approaching atoms, also influences $\Delta\Phi(z)$.

IV. DISCUSSION

Membrane proteins are influenced by the membrane environment which, complex and heterogeneous, includes lipids, water, and salt. In this paper we have chosen to investigate the interactions of water and salt in the vicinity of charged plates, which are intended as a model of the membrane. The main focus has been in determining how the salt and water behavior is different next to the plates than in bulk, which may ultimately lead to understanding how hydrated salt affects lipid–protein interactions. There is a good deal of experimental evidence which suggests that regulation of membrane surface charge density is a mechanism for controlling transmembrane protein structure and function.[10–14] One possible explanation is that there is an indirect biophysical pathway, which goes from the lipid, through the ordering of interfacial water and salt, to the protein. Therefore, it is important to study the details of water and salt behavior near
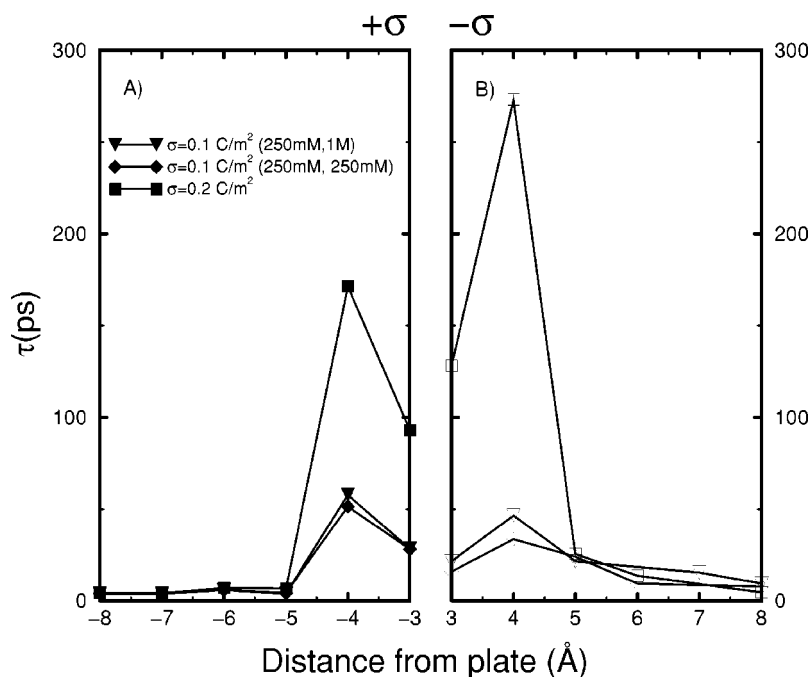
FIG. 7. Residency times, τ, for counterions as a function of distance from the charged plates, as calculated from Eq. (2.3). Shows sensitivity to changes in σ, but not to changes in negative plate side concentration. (A) Cl^- ions on the positive plate side (filled) and (B) Na^+ ions on the negative plate side (open). $\sigma = \pm 0.1$ C/m^2 (250 mM, 250 mM) (diamonds), $\sigma = \pm 0.1$ C/m^2 (250 mM, 1 M) (triangles), and $\sigma = \pm 0.2$ C/m^2 (squares) are shown.

membranes. Molecular dynamics simulations have been well suited for such studies. The charge densities used in the present study are realistic for biological membranes. The simulated 25.5 Å×25.5 Å area corresponds to two monolayers of approximately 9 lipid molecules each, which would have a charge density of -0.014 e/Å^2, or -0.22 C/m^2, if composed entirely of PS lipids. Thus, the molecular ordering which we have investigated in this work is presumably present in biomembrane systems as well. Such ordering is well documented in similar systems of electrolyte near single charged surfaces,[17–20,24,55,56] and provides the context for our discussion.

A. Asymmetric molecular ordering

The dominant electrostatic properties in these systems are the asymmetric partial charge distribution of the water molecule and the water–plate interactions. In a 250 mM NaCl solution there are only four salt molecules for every 988 water molecules, and hence one can easily see the importance of examining the role of water ordering and orientation. Water orientation probability distributions plotted in Fig. 3 agree with previously published simulation results[19,20] and it is remarkable that such agreement is seen despite significant differences in water parameters. Our system provides
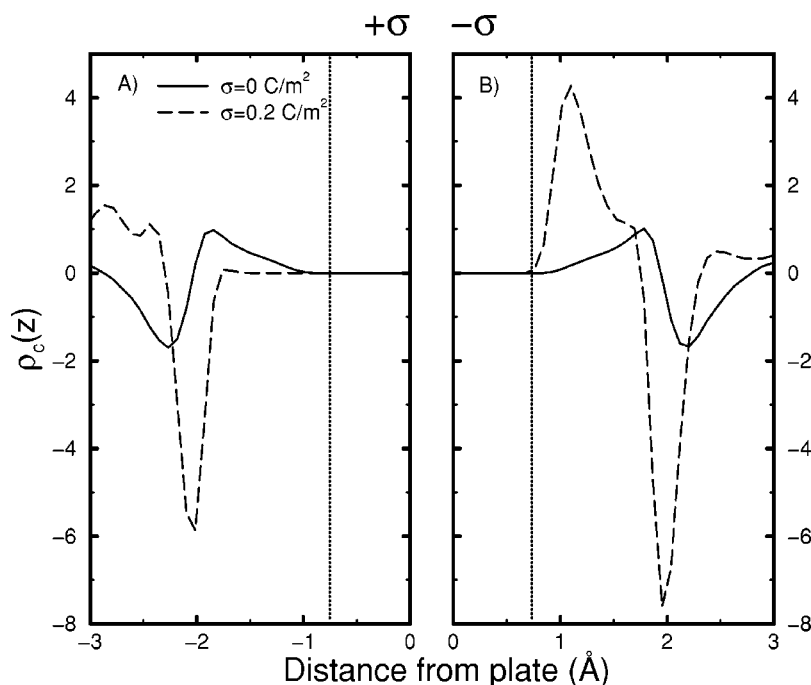

FIG. 8. Trajectory averaged charge density profiles, used to calculate the electrostatic potential profiles, are most sensitive to changes in σ. Note that, as described in the text, these distributions are dominated by water partial charges. (A) Positive plate side and (B) negative plate side charge density profiles as a function of distance from the plates for $\sigma = 0$ C/m^2 (solid line) and $\sigma = \pm 0.2$ C/m^2 (dashed line).
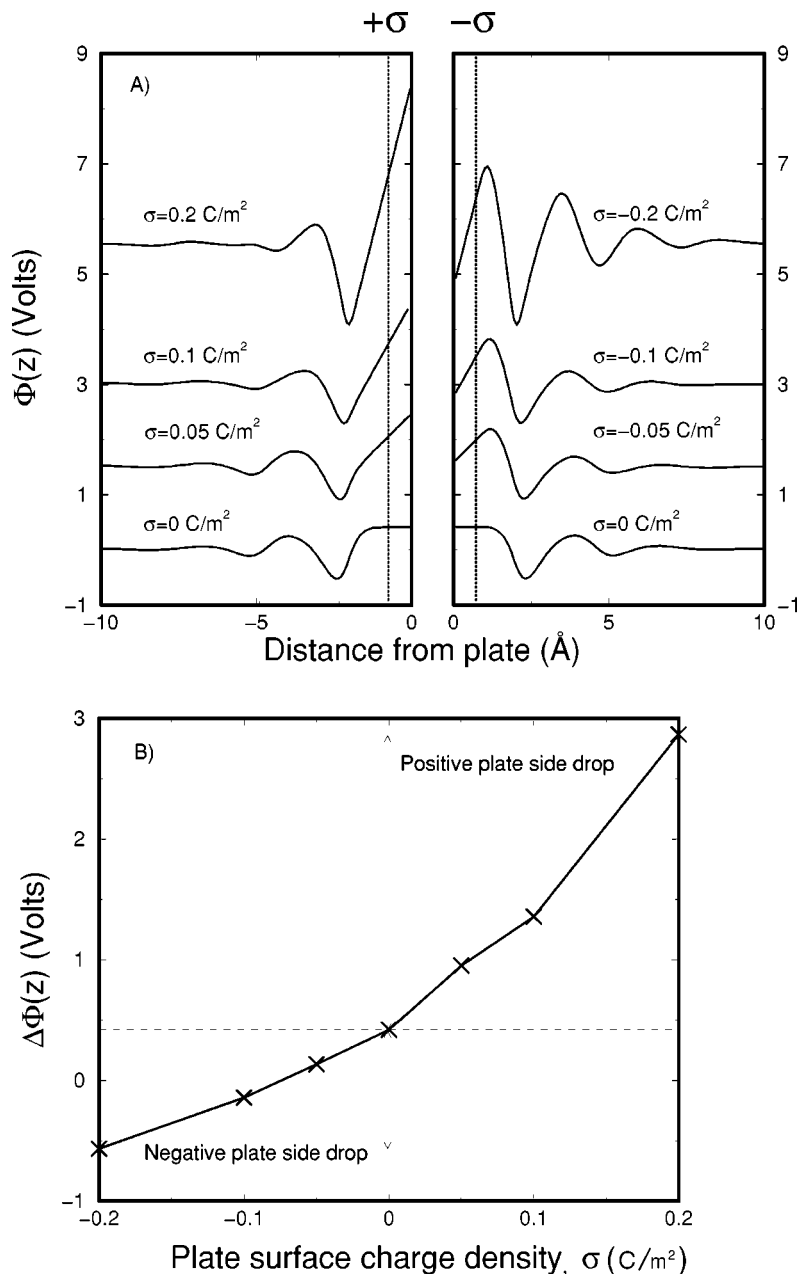
FIG. 9. Asymmetries are evident in the potential profiles calculated from Eq. (2). Potential as a function of distance from each plate is given in part (A) for four values of σ. Data has been shifted up for clarity. (B) Overall potential drop from the charged plate to bulk as a function of σ. The arrows highlight the asymmetric magnitude in potential drop from the oppositely charged plates.

the opportunity to investigate the behavior near two different surfaces within the same simulation, and as a result we have shown multiple examples of how the water geometric and electrostatic asymmetry results in asymmetry between the two sides.

The most obvious asymmetries between the two sides occur in the first layer of water and salt. Figure 10 recasts data from Figs. 2 and 5 to show an overlay of first layer oxygen, hydrogen, and counterion densities (Na^+ for the negative plate side, and Cl^- for the positive plate side). On the negative plate side, the Na^+ peak is clearly shifted away from the first layer water peaks, demonstrating that a well defined water layer intervenes between the plate and the first Na^+ layer. On the positive plate side, however, the Cl^- peak overlaps much more with the water peaks, suggesting a less discrete hydration layer. In order to more fully investigate the relative arrangements of the water and ions, and in order

to compare the behavior with the previous simulations of Spohr *et al.*,[21] Fig. 10(C) plots the distribution of oxygen–ion–oxygen angles (ζ) within the first hydration *shell* of each ion in these first water *layers*. The hydration shells are defined by the location of the minima in the $g(r)$ functions (data not shown). There is a clear geometric arrangement of waters around the Na^+ ions next to the negative plate, with the peak at $\cos \zeta = 0$ being consistent with an octahedral arrangement.[21] The water arrangement around the Cl^- ions on the positive plate side is much less well-defined, which is also consistent with the previous simulation results. As with the other asymmetric trends discussed above, the difference in hydration behavior increases with σ.

Understanding this asymmetric ordering of water and salt next to oppositely charged surfaces must include a discussion of how the insertion of neutral plates perturbs isotropic, bulk water. Under the influence of neither electrostatic nor vdW forces imposed by the plates, a bulk water molecule
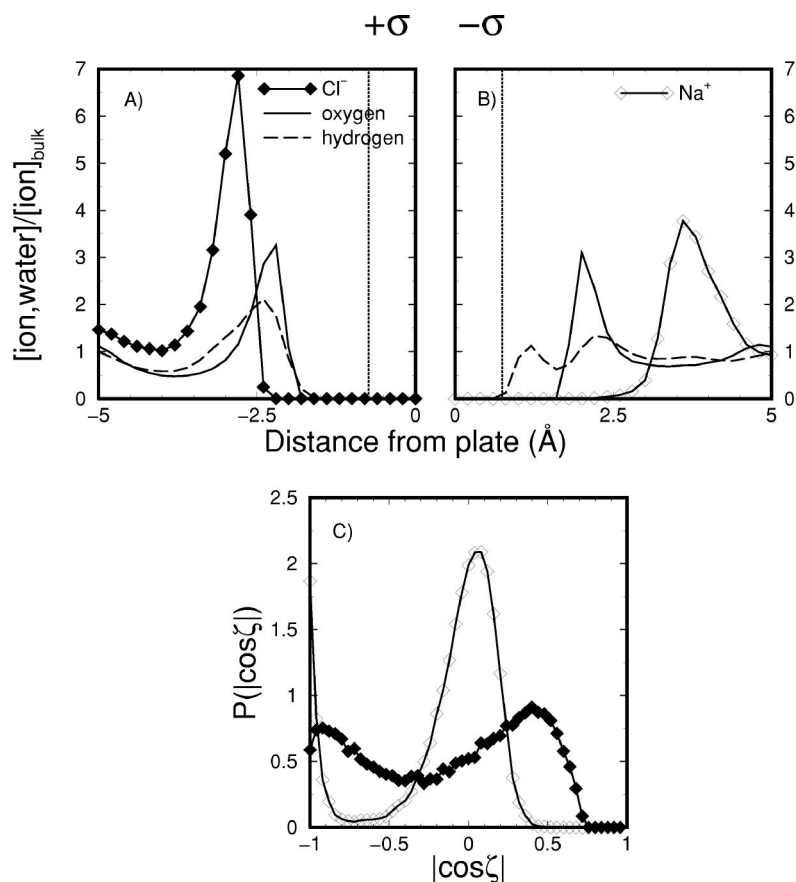
FIG. 10. Combined spatial distributions of water and salt reveal asymmetric ordering on the two sides of the system. Overlayed oxygen (—), hydrogen (– – –), (A) Cl⁻ (positive plate side, filled diamonds) and (B) Na⁺ (negative plate side, open diamonds) from the $\sigma=\pm0.1$ C/m^2 (250 mM, 250 mM) simulation. (C) Probability distribution of the O–ion–O angle in the first hydrations shell of the counterions in the first layer next to each plate [symbols as in parts (A) and (B)].

limit. It is important to point out that the resulting molecular distributions are dependent upon the reference point. If the reference is moved from the lab frame (plates, in this case) to a given water molecule, as is done for radial distribution functions, $g(r)$, oscillations are seen due to local water ordering. In fact, any insertion experiences the inherent local ordering of water. The resulting density distributions, $g(r)$, depend upon molecular interactions as well as molecular sizes. In this framework, one can think of the plates as insertions with infinite radii of curvature. Thus, we understand the origin of the oscillations in the $\sigma=0$ C/m^2 simulation, as reflecting this intrinsic property of the water–insertion interaction. In addition, we have seen that the smaller hydrogen atoms populate locations approximately 1 Å closer to the plates than do the oxygens, due to their smaller size. It should be noted that this hydrogen-plate packing is likely sensitive to the size and shape of the spheres which make up the plates, and by analogy the specific molecular nature of various biologically relevant lipid headgroups.

Oscillations in the number density profiles therefore reflect a *translational* ordering of the water molecules with respect to the plates. Beyond this type of ordering, we saw in Fig. 3 that waters respond to the insertion of the plates with *orientational* ordering as well. With no preferred orientation for bulk waters, the probability distribution of HH angles, as in Fig. 3, would be flat. Given that the insertion of neutral plates causes water reorientation, the question becomes: How does charging the plates affect this order? Figure 3(A) showed that the effect of increasing σ on the positive plate

side was to increase the population of waters with $\theta=90°$ (parallel to the plate). Such an orientation is favorable electrostatically, as it decreases the interaction between the positively charged hydrogen and the positive plate. Note that the ambiguity in this state (viz., H–O–H plane) is resolved by the charge density profile, $\rho_c(z)$ shown in Fig. 8, in that the first peak became more negative with increasing σ.

In contrast, the behavior seen in Fig. 3(B) for the negative plate side, showed a decrease in the water population with $\theta=90°$, suggesting that the favorable electrostatic interaction between the positively charged hydrogens and negatively charge plate is, surprisingly, diminished with increasing σ. However, the emerging peak in the $P(\cos\theta)$ distribution at $\theta=45°$ shifted towards the $\theta=90°$ state with increasing σ (data not shown). This is consistent with an increased electrostatic attraction of the hydrogen to the plate. Thus, there is clearly a delicate balance in forces acting on the water molecules on the negative plate side. The subtleties of this behavior may potentially be explained via a competition between sterics and electrostatic interactions. One notes that water is more cylindrical than spherical, with a length-to-width ratio of approximately 1.6 Å. The extent to which such a geometric asymmetry may influence entropic degrees of freedom, and hence the relative free energies of specific water orientations/packing arrangements, may depend upon the charge state of the plates (both sign and magnitude).

The asymmetry between the positive and negative plates was also seen in the salt behavior, again due to the interplay between ionic size and charge with water geometry and po-

larity. Na$^+$ residency times were significantly longer than those for Cl$^-$ next to their respective counter-charged plates. However, Cl$^-$ approaches its counter-charged plate more closely. Further, the water layers on the negative plate side were more well defined than those on the positive plate side. These phenomena may be explained by the formation of more well-defined hydration layers next to the Na$^+$, presumably facilitated by its smaller ionic radius. The presence of this more well-defined layer on the negative plate side increased Na$^+$ residency time and prevented Na$^+$ penetration to the plate. On the other hand, the larger Cl$^-$ ions disrupted these structures on the positive plate side, explaining the closer approach and shorter residency times.

B. Comparison to continuum theory

Efforts to capture water and salt behavior and interactions at the bilayer interface have been made using computationally efficient models such as the Gouy–Chapman extension of Poisson–Boltzmann theory. While continuum models have been quite illuminating,[68] we have seen that the molecular structure of water molecules, and subsequent ordering, has a dramatic influence on the shape of the electrostatic potential profiles. Such models do not capture the oscillations because of the dielectric treatment of the solvent. Despite this, continuum models have been extensively, and successfully, used to describe relevant experimental parameters, such as the Debye screening length of solvents of varying ionic strength. It is interesting, therefore, to attempt to extract related parameters from the oscillating profiles presented above in Fig. 9. As was done by Israelachvili[66] for calculating oscillations in solvation pressures acting at a solid–liquid interface, and elsewhere,[69] we have fit the potential as the product of an exponential decay and a periodic cosine function as follows:

$$\Phi(z) = A \exp\left(-\frac{z}{d}\right)\cos\left(\frac{2\pi(z-s)}{p}\right), \tag{4.1}$$

where A is the amplitude, d is a decay length, inspired by the Debye length, p is the period of the oscillations (giving peak spacing), and s is a phase shift setting the position of the peaks relative to the plate. Figure 11 compares the negative plate side potential profile for $\sigma = -0.2$ C/m^2 with this empirical model of the potential, with values of $A = 2.0$ V, $d = 3.0$ Å, $s = 1.1$ Å, and $p = 2.5$ Å. This value for p, it should be noted, is approximately the width of one water layer, which is consistent with the picture of water layering as the cause of the oscillations in the number density profiles. Further, the shift, s, can be related to the length of the exclusion zone in the vicinity of the plates. This empirical model clearly misses several details of the data, most notably the surface potential. It is interesting, nonetheless, to compare the value of d to the actual Debye length value, which is 6.08 Å for a 250 mM NaCl solution at 298 K. The value of d is thus approximately half of this in our model, which may be the result of the discreteness of water partial charges present in an all-atom representation of water, which is absent in the continuum model. Further refinements of these ideas are currently being explored in a new set of simulations.
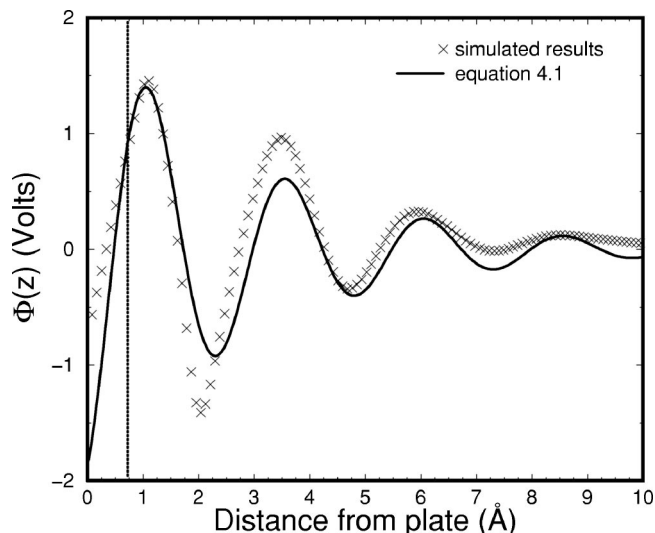

FIG. 11. A possible connection between the simulated results and continuum theory. Comparison of potential profile from the $\sigma = \pm 0.2$ C/m^2 simulation and the theoretical prediction calculated from Eq. (4.1). Parameters used are given in the text.

V. CONCLUSIONS

We have achieved two primary goals in the present study. First, we have applied the EW3DC methodology for calculating long-range electrostatics to a system with biologically relevant membrane geometry. We have successfully performed an all-atom simulation of a concentration gradient in such a geometry. Our results on water ordering are consistent with those from nonbilayer like systems, giving us confidence that the implementation of the EW3DC in this context successfully avoids interactions in the z-dimension, as is necessary for systems with two-dimensional periodicity. Second, with the viability of the method established, we aim to understand macroscopic features, such as the electrostatic potential, in terms of molecular-level ordering. We have shown that the geometric and electrostatic asymmetry of the water molecule is the fundamental basis for the macroscopic asymmetry between the two sides of a membranelike system.

The key role of molecular asymmetry in water ordering may impact upon the understanding of biological membranes. As we have performed simulations in the biological range of surface charge ($\sigma = 0$–0.2 C/m^2), our results are suggestive of the effect of changing the ratio of charged to uncharged lipids in biological membranes. As water structure around ions at the headgroup region of biological membranes has a profound impact on the fluctuations in headgroup order, our results regarding asymmetries are of interest.

We have initiated a series of related simulations in which the overall charge on each side of the system is nonzero. These new simulations, which will be discussed in a future report, should provide useful insight into how interactions between water and salt on opposite sides affect molecular ordering.

ACKNOWLEDGMENTS

[1] B. Hille, *Ionic Channels of Excitable Membranes* (Sinauer Associates, Sunderland, 1992).

[2] M. F. Brown and J. Seelig, Nature (London) **269**, 721 (1977).

[3] J. R. Rydall and P. M. Macdonald, Biochemistry **31**, 1092 (1992).

[4] M. Bloom, E. Evans, and O. G. Mouritsen, Q. Rev. Biophys. **24**, 293 (1991).

[5] M. F. Brown, Chem. Phys. Lipids **74**, 159 (1994).

[6] S. L. Keller, S. M. Gruner, and K. Gawrisch, Biochim. Biophys. Acta **1278**, 241 (1996).

[7] S. H. White and W. C. Wimley, Annu. Rev. Biophys. Biomol. Struct. **28**, 319 (1999).

[8] J. A. Killian and G. V. Heijne, Trends Biochem. Sci. **25**, 429 (2000).

[9] H. I. Petrache, D. M. Zuckerman, J. N. Sachs, J. A. Killian, R. E. Koeppe II, and T. B. Woolf, Langmuir **18**, 1340 (2002).

[10] H. J. Apell, E. Bamberg, and P. Lauger, Biochim. Biophys. Acta **552**, 369 (1979).

[11] W. N. Green and O. S. Anderson, Annu. Rev. Physiol. **53**, 341 (1991).

[12] T. K. Rostovtseva, V. M. Aguilella, I. Vodyanoy, S. M. Bezrukov, and V. A. Parsegian, Biophys. J. **75**, 1783 (1998).

[13] V. M. Aguilella and S. M. Bezrukov, Eur. Biophys. J. **30**, 233 (2001).

[14] E. Moczydlowski, O. Alvarez, C. Vergara, and R. Latorre, J. Membr. Biol. **83**, 273 (1985).

[15] G. Klose, K. Arnold, G. Peinel, H. Binder, and K. Gawrisch, Colloids Surf. **14**, 21 (1985).

[16] K. Gawrisch, D. Rustond, J. Zimmerberg, V. A. Parsegian, R. P. Rand, and N. Fuller, Biophys. J. **61**, 1213 (1992).

[17] D. Wei, G. N. Patey, and G. M. Torrie, J. Phys. Chem. **94**, 4260 (1990).

[18] H. Greberg and R. Kjellander, Mol. Phys. **83**, 789 (1994).

[19] J. P. Valleau and A. Gardner, J. Chem. Phys. **86**, 4162 (1987).

[20] G. Nagy, K. Heinzinger, and E. Spohr, Faraday Discuss. **94**, 307 (1992).

[21] E. Spohr, G. Toth, and K. Heinzinger, Electrochim. Acta **41**, 2131 (1996).

[22] K. Heinzinger, J. Mol. Liq. **73,74**, 239 (1997).

[23] E. Spohr, J. Chem. Phys. **107**, 6342 (1997).

[24] I. C. Yeh and M. L. Berkowitz, J. Chem. Phys. **111**, 3155 (1999).

[25] J. N. Glosli and M. R. Philpott, Electrochim. Acta **41**, 2145 (1996).

[26] P. S. Crozier, R. L. Rowley, E. Spohr, and D. Henderson, J. Chem. Phys. **112**, 9253 (2000).

[27] H. Heller, M. Schaefer, and K. Schulten, J. Phys. Chem. **97**, 8343 (1993).

[28] R. W. Pastor, Curr. Opin. Struct. Biol. **4**, 486 (1994).

[29] E. Egberts, S. J. Marrink, and H. J. C. Berendsen, Eur. Biophys. J. **22**, 423 (1994).

[30] S. W. Chiu, M. Clark, V. Balaji, S. Subramaniam, H. L. Scott, and E. Jakobsson, Biophys. J. **69**, 1230 (1995).

[31] S. E. Feller, Y. H. Zhang, and R. W. Pastor, J. Chem. Phys. **103**, 10267 (1995).

[32] S. Marrink, R. Sok, and H. J. C. Berendsen, J. Chem. Phys. **104**, 9090 (1996).

[33] W. Shinoda, M. Shimizu, and S. Okazaki, J. Phys. Chem. B **102**, 6647 (1998).

[34] T. B. Woolf and B. Roux, Proc. Natl. Acad. Sci. U.S.A. **91**, 11631 (1996).

[35] T. B. Woolf and B. Roux, Proteins **24**, 92 (1997).

[36] D. P. Tielman, M. S. P. Sansom, and H. J. C. Berendsen, Biophys. J. **76**, 1757 (1999).

[37] Z. Qi and M. Sokabe, Biophys. Chem. **82**, 183 (1999).

[38] L. R. Forrest, A. Kukol, I. Arkin, D. P. Tielman, and M. S. P. Sansom, Biophys. J. **78**, 79 (2000).

[39] I. Shrivastava and M. Sansom, Eur. Biophys. J. **31**, 207 (2002).

[40] A. Grossfield, J. Sachs, and T. B. Woolf, Proteins **41**, 211 (2000).

[41] G. S. Delbound, T. S. Cohen, and P. Rossky, J. Mol. Liq. **60**, 221 (1994).

[42] L. Perera, U. Essmann, and M. L. Berkowitz, J. Chem. Phys. **102**, 450 (1995).

[43] J. E. Roberts and J. Schnitker, J. Phys. Chem. **99**, 1322 (1995).

[44] S. G. Kalko, G. Sese, and J. A. Padro, J. Chem. Phys. **104**, 9578 (1996).

[45] K. V. Damodaran and K. M. Merz, Langmuir **9**, 1179 (1993).

[46] L. Perera, U. Essmann, and M. L. Berkowitz, Langmuir **12**, 2625 (1996).

[47] D. E. Parry, Surf. Sci. **49**, 433 (1975).

[48] D. M. Heyes, M. Barber, and J. H. R. Clarke, J. Chem. Soc., Faraday Trans. 2 **73**, 1485 (1977).

[49] S. W. de Leeuw and J. W. Perram, Mol. Phys. **37**, 1313 (1979).

[50] I. C. Yeh and M. L. Berkowitz, Chem. Phys. Lett. **301**, 81 (1999).

[51] S. Y. Liem and J. H. R. Clarke, Mol. Phys. **92**, 19 (1997).

[52] A. H. Widmann and D. B. Adolf, Comput. Phys. Commun. **107**, 167 (1997).

[53] E. R. Smith, Proc. R. Soc. London, Ser. A **375**, 475 (1981).

[54] J. Hautman, J. W. Halley, and Y. J. Rhee, J. Chem. Phys. **91**, 467 (1989).

[55] P. S. Crozier, R. L. Rowley, and D. Henderson, J. Chem. Phys. **113**, 9202 (2000).

[56] S. H. Lee and P. J. Rossky, J. Chem. Phys. **100**, 3334 (1994).

[57] J. F. Nagle and S. Tristram-Nagle, Biochim. Biophys. Acta **1469**, 159 (2000).

[58] B. Roux and M. J. Karplus, J. Comput. Chem. **16**, 690 (1995).

[59] B. R. Brooks, R. E. Bruccoleri, B. D. Olafson, D. J. States, S. Swaminathan, and M. J. Karplus, J. Comput. Chem. **4**, 187 (1983).

[60] W. L. Jorgensen, J. Chandrasekhar, J. D. Madura, R. W. Impey, and M. L. Klein, J. Chem. Phys. **79**, 926 (1983).

[61] A. D. MacKerrel, Jr. *et al.*, J. Phys. Chem. B **102**, 3586 (1998).

[62] A. D. MacKerrel and S. E. Feller, J. Phys. Chem. B **31**, 7510 (2000).

[63] C. L. Brooks and M. J. Karplus, J. Chem. Phys. **79**, 6312 (1983).

[64] E. Oyen and R. Hentschke, Langmuir **18**, 547 (2002).

[65] M. Gerstein, J. Tsai, and M. Levitt, J. Mol. Biol. **249**, 955 (1995).

[66] J. N. Israelachvili, *Intermolecular and Surface Forces* (Academic, London, 1992).

[67] J. Zimmerberg and V. A. Parsegian, Nature (London) **323**, 36 (1986).

[68] R. M. Peitzsch, M. Eisenberg, K. A. Sharp, and S. McLaughlin, Biophys. J. **68**, 729 (1995).

[69] L. R. Pratt, J. Phys. Chem. **96**, 25 (1992).